NANO LETTERS

pubs.acs.org/NanoLett Letter

Phase-Controlled Synthesis of Ru Nanocrystals via Template-Directed Growth: Surface Energy versus Bulk Energy

Annemieke Janssen, Zhiheng Lyu, Marc Figueras-Valls, Hsin-Yun Chao, Yifeng Shi, Veronica Pawlik, Miaofang Chi, Manos Mavrikakis,* and Younan Xia*

Cite This: *Nano Lett.* 2022, 22, 3591−3597 Read Online

ACCESS | Metrics & More | Article Recommendations | Supporting Information

ABSTRACT: Despite the successful control of crystal phase using template-directed growth, much remains unknown about the underlying mechanisms. Here, we demonstrate that the crystal phase taken by the deposited metal depends on the lateral size of face-centered cubic (*fcc*)-Pd nanoplate templates with 12 nm plates giving *fcc*-Ru while 18−26 nm plates result in hexagonal closed-packed (*hcp*)-Ru. Although Ru overlayers with a metastable *fcc*- (high in bulk energy) or stable *hcp*-phase (low in bulk energy) can be epitaxially deposited on the basal planes, the lattice mismatch will lead to jagged *hcp*- (high in surface energy) and smooth *fcc*-facets (low in surface energy), respectively, on the side faces. As the proportion of basal and side faces on the nanoplates varies with lateral size, the crystal phase will change depending on the relative contributions from the surface and bulk energies. The Pd@*fcc*-Ru outperforms the Pd@*hcp*-Ru nanoplates toward ethylene glycol and glycerol oxidation reactions.

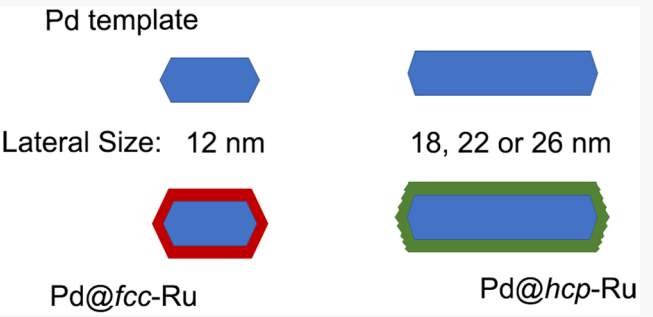

KEYWORDS: *metal nanocrystal, crystal phase, metastable phase, structure−property relationship, polymorphism*

Over the past two decades, colloidal synthesis of metal nanocrystals has steadily improved in terms of shape control. Consequently, this parameter can now be systematically tailored to optimize the performance of colloidal metal nanocrystals in various applications, including catalysis, photonics, electronics, and biomedicine.[1−3] For example, Pd nanocrystals with cubic, octahedral, icosahedral, and right bipyramidal shapes have been synthesized and compared as electrocatalysts toward formic acid oxidation (FAO).[4−6] The {100} facets on cubic nanocrystals were found to be almost two times as active as the {111} facets on octahedral nanocrystals, while twin boundaries could additionally enhance the catalytic activity.[4,5] This and many other examples demonstrate the importance of surface engineering in determining the catalytic properties of metal nanocrystals.[1,7−9] In comparison, polymorphism has been largely overlooked as a synthetic avenue. While most of the metals are naturally found in one thermodynamically stable crystal phase, their nanocrystals can also be prepared to feature metastable crystal structures.[10] Control over this characteristic, known as polymorphism, might unlock a new knob for creating nanocrystals with enhanced or new properties.

Recently, various nanocrystals have been fabricated in metastable crystal phases. Methods include kinetically controlled one-pot synthesis, template-directed growth, and pressure-induced phase transition.[7] Early examples include the synthesis of hexagonal close-packed (*hcp*) and 4H- Au and Ag, alongside more recent reports of *hcp*-Rh and *hcp*-Pd.[11−16] Unlike other noble metals, which typically display a face-centered cubic (*fcc*) structure, Ru is naturally found in the *hcp* phase, providing an intriguing system to investigate polymorphism.[17] Metastable *fcc*-Ru nanoparticles were first obtained in a one-pot synthesis, where a proper combination of solvent and coordinating ligand was used to enable the observation of polymorphism.[18,19] Recently, *fcc*-Ru was prepared using template-directed growth, where preformed nanocrystals in a well-defined crystal phase serve as seeds to direct the deposition of a different metal.[20] Under proper conditions, the resulting shell will take on the crystal lattice of the template to give a metastable core−shell structure. When Ru atoms were deposited on *fcc*-Pd templates with different shapes, the shell took an *fcc* structure while assuming the template's shape.[21−25] Such metastable nanocrystals were active toward various catalytic reactions, including the reduction of p-nitrophenol, dehydrogenation of ammonia borane, hydrazine decomposition, and possibly nitrogen reduction.[21−25] While these studies demonstrated the capa-

Received: December 28, 2021
Revised: April 14, 2022
Published: April 19, 2022

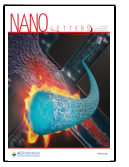

Downloaded via GEORGIA INST OF TECHNOLOGY on June 20, 2022 at 20:58:09 (UTC).
See https://pubs.acs.org/sharingguidelines for options on how to legitimately share published articles.

ACS Publications © 2022 American Chemical Society

https://doi.org/10.1021/acs.nanolett.1c05009
Nano Lett. 2022, 22, 3591−3597

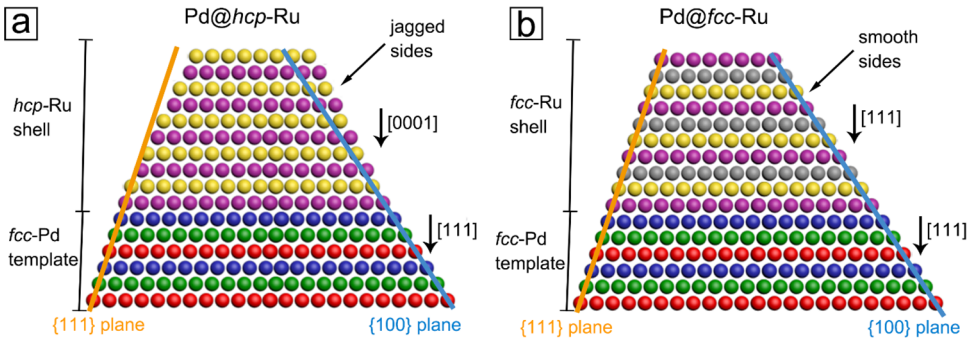

Figure 1. (a) Model depicting how the {111} and {100} planes from the *fcc*-Pd template cannot smoothly cut through an *hcp*-Ru shell, leading to jagged side faces. (b) Model depicting how the {111} and {100} planes from the *fcc*-Pd template can smoothly cut through an *fcc*-Ru shell, leading to smooth side faces.

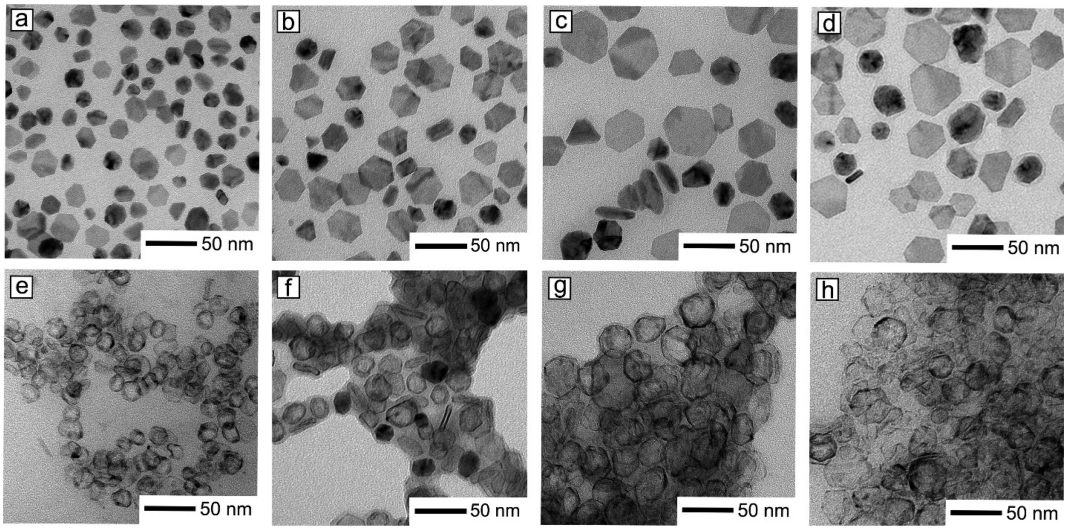

Figure 2. TEM images of (a) 12 nm, (b) 18 nm, (c) 22 nm, and (d) 26 nm Pd@Ru nanoplates, and (e–h) the corresponding Ru nanocages after selective etching of Pd from the core.

bility and versatility of template-directed growth, much remains to be discovered with regard to the mechanisms responsible for controlling the crystal phase. For example, it remains elusive how template size will affect the outcome of a template-directed synthesis.[7,17,20]

This study aims to investigate the effect of template size on the crystal phase taken by nanocrystals formed through template-directed growth. We chose Pd nanoplates as the template because the area proportion of their side faces is strongly dependent on the lateral size. Specifically, a nanoplate is terminated in {111} facets at the two basal planes whereas its side faces are enclosed by a mix of {111} and {100} facets with their arrangement determined by the twin structure.[26,27] Regardless of the twin structure, it is impossible to generate a perfect *hcp*-Ru shell on an *fcc*-Pd nanoplate. Since the {111} facets of an *fcc* structure have C3 symmetry that matches the {0001} facets of an *hcp* lattice, *hcp*-Ru overlayers can be readily deposited on the basal planes.[28] However, the *hcp*-Ru overlayers cannot be smoothly extended over the side faces, as the ABAB sequence characteristic of *hcp* stacking is not aligned with the ABCABC stacking of the underlying *fcc* lattice. This mismatch inevitably results in a compliance issue between the *hcp*-shell and *fcc*-template. In other words, when depositing *hcp*-Ru on an *fcc*-Pd nanoplate, the planes corresponding to the {111} and {100} facets on the side faces cannot smoothly cut through the *hcp*-Ru shell (Figure 1a). Therefore, although *hcp*-Ru overlayers can epitaxially grow from the basal planes, the side faces will experience significant roughening and become jagged.[17,28] The large number of undercoordinated atoms will increase the surface energy, even though the bulk energy can be kept low due to the formation of *hcp*-Ru, a thermodynamically favorable phase.

Alternatively, the deposited Ru atoms can take an *fcc* structure. Overlayers of *fcc*-Ru can also be readily deposited on the basal plane of an *fcc*-Pd nanoplate with minimal lattice mismatch.[23,28] Additionally, {111} and {100} planes of the side faces can neatly cut through the *fcc* shell (Figure 1b). Thus, with an *fcc*-Ru shell, the side faces form a smooth surface with few undercoordinated atoms, which helps keep the surface energy low.[17] However, since *fcc*-Ru is metastable, the bulk energy will increase relative to the thermodynamically stable *hcp*-Ru.[7] Taken together, by changing the lateral size of the basal plane (resulting in smooth growth for both *hcp*- and *fcc*-Ru) while keeping the side faces constant in area (resulting in either smooth or jagged surfaces), we expect to vary the relative contributions from the surface and bulk energies to manipulate the crystal phase taken by the template-directed Ru shells.

To investigate the effect of lateral size, we synthesized and characterized Pd@Ru core–shell nanocrystals grown from Pd

https://doi.org/10.1021/acs.nanolett.1c05009
Nano Lett. 2022, 22, 3591–3597

nanoplates with different edge lengths. A published protocol was modified to obtain Pd nanoplates with edge lengths of 12.15 ± 0.88, 18 ± 1.21, 22.38 ± 1.88, and 26.46 ± 1.62 nm.[29] The nanoplates had an average thickness of 4.6 nm, alongside standard deviations of 0.33, 0.48, 0.41, and 0.50 nm, respectively. The nanoplates were used as templates for the overgrowth of Ru to give Pd@Ru core−shell nanoplates of 8.41 ± 0.47, 8.56 ± 0.49, 8.53 ± 0.56, and 8.68 ± 0.62 nm, respectively, in thickness (Figure 2a−d). When the Pd@Ru particles were etched to selectively remove the Pd core, well-defined nanocages were obtained, confirming the complete epitaxial overgrowth of Ru on both basal and side faces (Figure 2e−h).[22] The structures after etching were nanocages rather than nanoframes. When the amount of the deposited Ru was increased, the Pd core could no longer be etched, indicating that the thick Ru shell blocked the etchant from accessing the underlying Pd.[30] For nanoframes, we expect a concave surface upon deposition of a large amount of Ru, rather than a flat surface, while the Pd core would remain accessible by the etchant.[31]

Next, we analyzed the Pd@Ru nanoplates by X-ray diffraction (XRD) to determine the effect of particle size on the crystal structure taken by the Ru (Figure 3). For the 12 nm

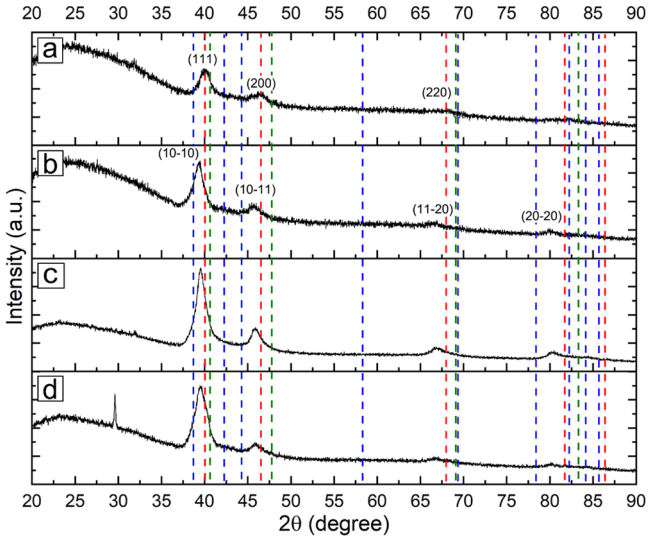

Figure 3. XRD patterns of (a) 12 nm, (b) 18 nm, (c) 22 nm, and (d) 26 nm Pd@Ru nanoplates, indicating an *fcc* phase for the 12 nm Pd@Ru nanoplates, and an *hcp* phase for the larger nanoplates. The red, blue, and green dashed lines correspond to the characteristic peaks of *fcc*-Pd (JCPDS No. 05-0685), *hcp*-Ru (JCPDS No. 06-0663), and *fcc*-Ru (JCPDS No. 01-088-2333), respectively.

sample, the XRD pattern is indicative of *fcc*-Ru, suggesting successful template-directed deposition.[18,32] The main XRD peak around 40.2° is between the *fcc*-Pd and *fcc*-Ru reference peaks, likely due to tensile lattice strain experienced by the {111} planes of *fcc*-Ru on the {111} planes of *fcc*-Pd, shifting the peak to smaller angles. This peak should arise from the Ru shell only because the signal from the *fcc*-Pd core would appear as a shoulder or secondary peak.[16] Similarly, the lack of a shoulder peak for *hcp*-Ru indicates that the shell should be consistently made of *fcc* on both the basal and side faces. Additionally, fast Fourier transform (FFT) analysis and lattice fringe spacing from high-resolution transmission electron microscopy (HR-TEM) images of the 12 nm Pd@Ru nanoplates indicate that the basal planes are *fcc*-Ru {111} facets, while the lattice spacing on the side faces can be assigned to the {111} and {200} planes of *fcc*-Ru (Figure S1a,d). For the 18−26 nm Pd@Ru samples, the main XRD peak was closer to the *hcp*-Ru reference, suggesting that the Ru shell retained its *hcp*-structure. The peak location between the *hcp*-Ru and *fcc*-Pd references results from the compressive lattice strain arising from the mismatch between the {111} planes of *fcc*-Pd and the {0001} planes of *hcp*-Ru, shifting the peak to larger angles.[33] The FFT and lattice spacings for the 22 and 26 nm Pd@Ru nanoplates indicate that the basal planes are {0001} facets of *hcp*-Ru, while high-index *hcp* facets comprise the side faces (Figure S1b-c, e-f). Altogether, these results validate that the particle size is an important factor in template-directed synthesis, with small nanoplates favoring the metastable *fcc*-Ru while large nanoplates revert to conventional *hcp*-Ru.

As the nanoplates grow laterally, the surface area of the basal planes increases more quickly than that of the side faces.[27] Consequently, large Pd nanoplates have a much greater proportion of basal planes compared to side faces, and the latter will only contribute a small fraction to the overall surface area. Thus, the lower bulk energy associated with *hcp*-Ru on the large basal planes might balance out the increase in surface energy arising from the presence of the jagged side faces. In contrast, for small nanoplates, the greater proportion of side faces makes it energetically favorable to keep the surface energy low through the formation of smooth side faces at the expense of generating metastable *fcc*-Ru.[17] Therefore, the phase change that occurs between 12- and 18 nm Pd@Ru nanoplates could be attributed to a shift in dominance between the bulk and surface energies due to the relative proportions of basal planes and side faces.

Beyond particle size, we also investigated the effects of growth mode, shell thickness, injection rate, and reaction temperature.[20] First, to determine the deposition mode of the Ru phase, samples of 12 nm Pd plates were taken every 2 h over a 17 h synthesis to analyze the growth process (Figure S2). At no point was cluster formation observed on the particles, indicating constant epitaxial growth. This observation suggests that the diffusion rate must have been faster than the deposition rate, leading to a layer-by-layer growth mode.[34]

Additionally, the shell thickness needs to be controlled in template-directed growth. The thickness can be estimated by measuring the difference between the thicknesses of the plain 12 nm Pd and the corresponding Pd@Ru nanoplates. The 12 nm Pd nanoplates had an average thickness of 4.6 nm. By increasing the precursor amount, the thickness of the Pd@Ru nanoplates was increased to 8.41, 9.21, and 11.59 nm, respectively, corresponding to shells of about 10, 12, and 18 atomic layers (Figure 4). On the basis of XRD spectra, the Ru shell took an *fcc* phase up to 10 atomic layers before reverting to *hcp*-Ru for thicker shells, likely due to a shift from layer-by-layer to island growth.[22,35,36] The higher metal precursor concentration increases the deposition rate, while the diffusion rate remains the same.[36] Thus, additional atoms can deposit on the nanoplate before the previous ones can diffuse away, leading to *hcp*-Ru islands and eventually an *hcp*-Ru shell. Similarly, template-directed growth depends on a slow precursor injection rate. While a 0.5 mL/h injection rate gave epitaxial deposition, the Ru shell became bumpy, indicative of island growth, when the rate was increased to 1 or 2 mL/h (Figure S3). Faster injection led to higher precursor

https://doi.org/10.1021/acs.nanolett.1c05009
Nano Lett. 2022, 22, 3591−3597

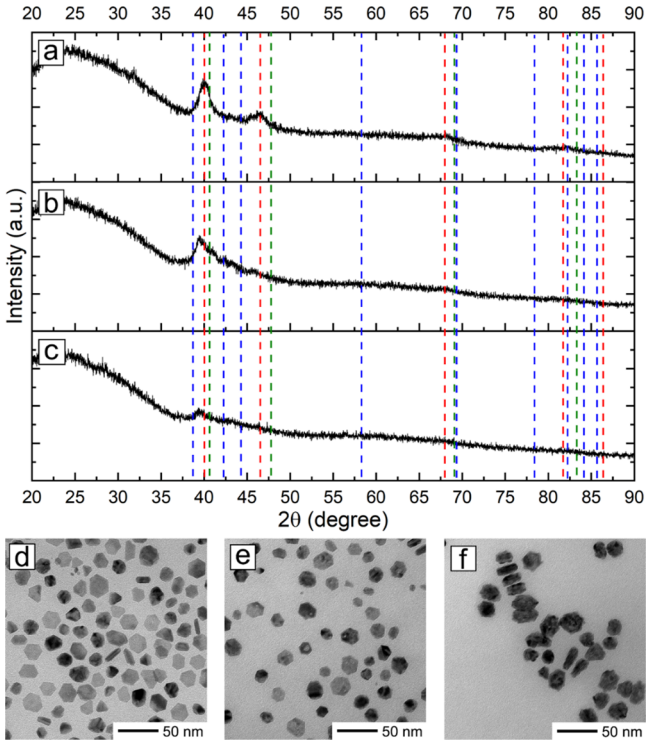

Figure 4. (a−c) XRD patterns and (d−f) TEM images recorded from 12 nm Pd@Ru nanoplates with different total thicknesses: (a,d) 8.41, (b,e) 9.21, and (c,f) 11.59 nm. The red, blue, and green dashed lines correspond to the characteristic peaks of *fcc*-Pd, *hcp*-Ru, and *fcc*-Ru, respectively.

concentrations, changing the growth mode by affecting the relative rates of diffusion and deposition, as described above.[34] Together, successful template-directed synthesis is reliant on thin shells generated under relatively slow injection of the precursor.

Next, we determined the effect of reaction temperature on shell deposition (Figure S4). When the reaction temperature was decreased from the standard 180 to 165 °C, the nanocages were thinner due to inadequate reduction of the Ru precursor. With a further decrease to 150 °C, no particles were observed after Pd etching, as negligible Ru was deposited on the Pd nanoplates due to the low reducing power of ethylene glycol (EG) at this temperature.[37,38] With an increase to 190 °C, there was no noticeable change relative to the standard protocol. Although high temperatures should speed up both the deposition and diffusion of Ru, the deposition rate was limited by the slow injection rate of the precursor.[34] The slow deposition and fast diffusion would result in Pd@Ru nanoplates identical to those from the standard protocol.

To elucidate the mechanistic details involved in the phase-control, we conducted density functional theory (DFT) calculations (Figures S5−S8, Tables S1−S6). The overall energy of the Pd@Ru system should directly depend on the relative energetic contributions from the *hcp*- and *fcc*-Ru phases and the surface areas of the different faces. Accordingly, the displayed Ru phase would be the one that minimizes the total energy of the system, where the total energy for a given Ru phase can be calculated as the sum of energies of the various independent faces weighted by their surface areas

$$E_{\text{total-phaseX}} = A_{\text{side}\{111\}} \times E_{\text{X-side}\{111\}} + A_{\text{side}\{100\}} \times E_{\text{X-side}\{100\}} + A_{\text{basal}\{111\}} \times E_{\text{X-basal}\{111\}} \quad (1)$$

where X can be the *hcp*- or *fcc*-Ru phase, and each energy term combines the surface, bulk, and interface contributions. Another representation for the previous expression subtracts the total energies for the different Ru phases

$$\Delta E_{\text{total}} = A_{\text{side}\{111\}} \times (E_{\text{hcp-side}\{111\}} - E_{\text{fcc-side}\{111\}}) + A_{\text{side}\{100\}} \times (E_{\text{hcp-side}\{100\}} - E_{\text{fcc-side}\{100\}}) + A_{\text{basal}\{111\}} \times (E_{\text{hcp-basal}\{111\}} - E_{\text{fcc-basal}\{100\}}) \quad (2)$$

where a positive or negative difference would indicate that the *fcc*- or *hcp*-Ru phase is preferred, respectively. A detailed description of the calculations can be found in the Supporting Information, with only the main conclusions presented below.

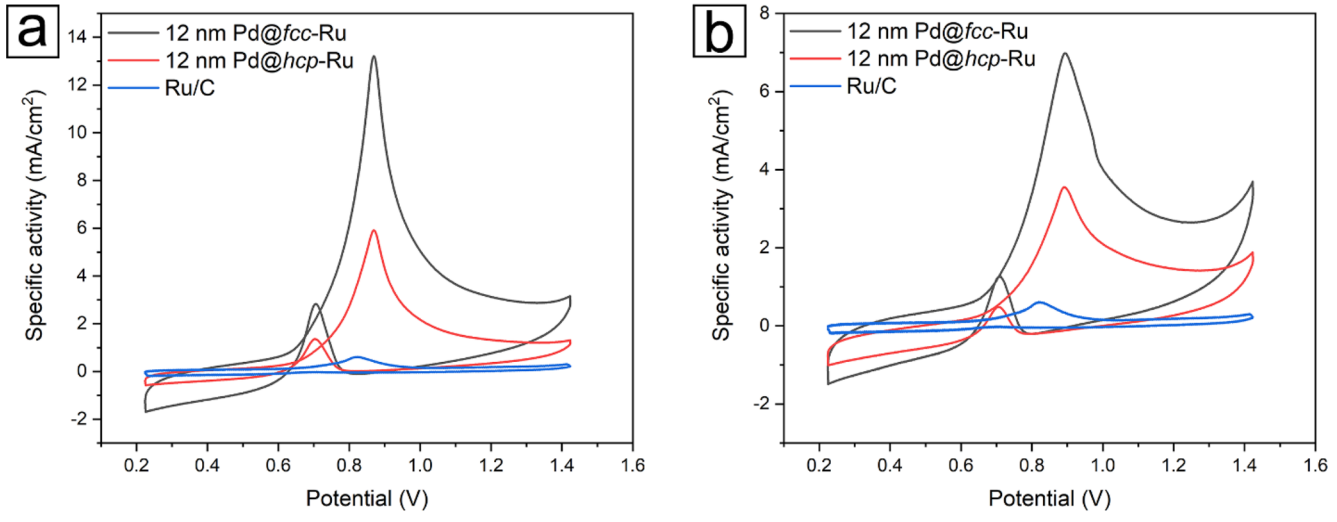

Figure 5. (a) CV curves for EGOR on the 12 nm Pd@*fcc*-Ru nanoplates, 12 nm Pd@*hcp*-Ru nanoplates, and *hcp*-Ru/C, recorded in an Ar-saturated solution containing 1 M KOH and 1 M EG. The current density was normalized to the corresponding ECSA. (b) CV curves for GlyOR on the 12 nm Pd@*fcc*-Ru nanoplates, 12 nm Pd@*hcp*-Ru nanoplates, and *hcp*-Ru/C, recorded in an Ar-saturated solution containing 1 M KOH and 1 M glycerol. The current density was normalized to the corresponding ECSA.

https://doi.org/10.1021/acs.nanolett.1c05009
Nano Lett. 2022, 22, 3591−3597

The computational results indicate that the Pd@*hcp*-Ru is more stable than the Pd@*fcc*-Ru on the basal planes, as shown in Table S1, supporting the proposed hypothesis. Nevertheless, the acquired results in Table S1 do not show any face on which the *fcc*-Ru phase is more stable than its *hcp*-Ru counterpart, disagreeing with the reported experimental trends. However, the computations resorted to several approximations and assumptions in order to feasibly study a nontrivial problem. As such, the reported conclusions cannot plainly prove or disprove the thermodynamic explanation for Ru phase control. Our computational approach relies on interfacial models that could not adequately capture the complexity of these physical systems. For instance, the models used for the side interfaces (see SI for description) were acquired by cutting through the continuous *hcp*-Ru phase and looking for translational symmetry so as to preserve the idea of a continuous growth for the whole nanoplate; however, such consideration could lead to unrealistic models if reconstructions are present in the side faces. Additionally, strain effects have been included in the computational approach, however, the experimentally observed compressive strain for the *hcp*-Ru phase cannot be easily modeled in a stoichiometric regime, as the actual mismatch between Ru (smaller lattice parameter) and Pd (larger lattice parameter) faces will lead to unreasonable lattice parameters smaller than those naturally observed for both species in order to produce compressive strains on the *hcp*-Ru phase. An alternative explanation may arise from nonstoichiometric interfaces with stoichiometry of Ru:Pd atoms at the interface greater than one,[39,40] but the computational cost of capturing such effects goes beyond the scope of this study. Finally, considering computationally convenient small models for each facet would not account for the complexities present in the Pd@Ru nanoplates, such as vertices, edges, stacking faults, and defects that affect the overall energy balance.

Finally, we investigated the catalytic capabilities of the Pd@Ru nanoplates toward the ethylene glycol oxidation reaction (EGOR) and glycerol oxidation reaction (GlyOR). EGOR and GlyOR are both essential for the operation of alcohol-based fuel cells and require a catalyst that is commonly based on Pt.[41] To evaluate their activities, the 12 nm Pd@Ru nanoplates were loaded on carbon at about 20 wt % with *hcp*-Ru nanoparticles serving as a reference. Figure 5 shows both the anodic and cathodic CV scans for EGOR and GlyOR. The activity of the 12 nm Pd@Ru nanoplates showed a dependence on the crystal phase, whereas the *hcp*-Ru nanoparticles showed negligible activity. Thus, the interaction between the Ru shell and the Pd core must promote the activity of the Pd@Ru nanoplates. Previous studies indicated that *hcp*-Ru was not active toward EGOR or GlyOR, while Pd was quickly deactivated due to poisoning by CO.[41,42] The poisoning during both reactions could be mitigated due to a favorable bimetallic interactions, as the active-site blocking CO can be readily removed in the presence of oxygen species on Ru.[42,43] Additionally, a thin Ru shell (about 3−4 atomic layers) promotes beneficial strain and electronic effects between the core and shell.[41,44] The ligand effect between the Pd and Ru aids the C−C bond breaking that is essential to alcohol oxidation, while promoting charge transfer, weakening the CO bonding strength, and helping to remove poisoning carbonate species.[41,42,45−47] Altogether, the Pd core can significantly enhance the catalytic activity of Ru shell toward alcohol oxidation.

The EGOR and GlyOR activities were also sensitive to the Ru phase, as the *fcc*-Ru shells outperformed *hcp*-Ru. For EGOR, the 12 nm Pd@Ru nanoplates with *hcp* or *fcc* structures had specific peak activities of 5.87 and 13.19 mA/cm^2 at 0.871 V versus the reversible hydrogen electrode (RHE), respectively. For GlyOR, the *hcp*- and *fcc*- shells displayed 3.54 and 6.97 mA/cm^2 at 0.89 V_{RHE}. The improved catalytic activity of *fcc*-Ru toward alcohol oxidation might result from improved durability due to decreased poisoning.[43,45] Previously, *fcc*-Ru was shown to be more active toward CO oxidation compared to *hcp*-Ru, thereby reducing CO poisoning and resulting in more exposed active sites.[18,42] Additionally, for alcohol oxidation, tensile strain might promote catalytic activity by aiding the electron transfer between the core and shell, while simultaneously improving the interaction between the reagents and catalyst surface.[48] This trend indicates that the tensile strain experienced by the Pd@*fcc*-Ru particles is beneficial to EGOR and GlyOR, unlike the compressive strain on Pd@*hcp*-Ru particles. These examples show that template-directed growth is a powerful technique to obtain catalytically active nanoparticles through affecting surface atomic arrangement, lattice strain, and novel core−shell interactions.[7,32,42,43,48] The potential of phase-controlled core−shell nanocrystals for catalysis highlights the importance in understanding their growth mechanisms.

Altogether, we systematically investigated the effects of various synthetic parameters on the crystal phase taken by Ru shells deposited on Pd nanoplates. Our experimental results suggest that the lateral size of the template impacts the crystal phase, as the Ru shells take on the metastable *fcc* structure on 12 nm plates while reverting to the stable *hcp* lattice on 18−26 nm plates. This outcome was attributed to a shift in dominance between surface and bulk energies corresponding to the proportions of the basal planes and side faces, although not supported by computations. A slow injection rate, thin shells below about 10 atomic layers, and a high reaction temperature are all required for achieving conformal, layer-by-layer growth. When the 12 nm Pd@Ru nanoplates are evaluated toward EGOR and GlyOR, the Pd@*fcc*-Ru outperforms both the *hcp* counterpart and the *hcp*-Ru nanoparticles in terms of specific activity. Altogether, this study sheds light on the mechanism involved in the template-directed growth of metal nanocrystals with different phases, moving toward rational and deterministic synthesis.

■ ASSOCIATED CONTENT

Supporting Information

The Supporting Information is available free of charge at https://pubs.acs.org/doi/10.1021/acs.nanolett.1c05009.

Experimental methods, computational details, and additional figures for mechanistic details and electrochemical data (PDF)

■ AUTHOR INFORMATION

Corresponding Authors

Manos Mavrikakis − *Department of Chemical and Biological Engineering, University of Wisconsin-Madison, Madison, Wisconsin 53706, United States*; Email: manos@engr.wisc.edu

Younan Xia − *School of Chemistry and Biochemistry, Georgia Institute of Technology, Atlanta, Georgia 30332, United States; The Wallace H. Coulter Department of Biomedical Engineering, Georgia Institute of Technology and Emory University, Atlanta, Georgia 30332, United States;*

https://doi.org/10.1021/acs.nanolett.1c05009
Nano Lett. 2022, 22, 3591−3597

orcid.org/0000-0003-2431-7048; Email: younan.xia@bme.gatech.edu

Authors

Annemieke Janssen − *School of Chemistry and Biochemistry, Georgia Institute of Technology, Atlanta, Georgia 30332, United States;* orcid.org/0000-0002-7721-597X

Zhiheng Lyu − *School of Chemistry and Biochemistry, Georgia Institute of Technology, Atlanta, Georgia 30332, United States;* orcid.org/0000-0002-1343-4057

Marc Figueras-Valls − *Department of Chemical and Biological Engineering, University of Wisconsin-Madison, Madison, Wisconsin 53706, United States*

Hsin-Yun Chao − *Center for Nanophase Materials Sciences, Oak Ridge National Laboratory, Oak Ridge, Tennessee 37831, United States*

Yifeng Shi − *School of Chemical and Biochemical Engineering, Georgia Institute of Technology, Atlanta, Georgia 30332, United States*

Veronica Pawlik − *School of Chemistry and Biochemistry, Georgia Institute of Technology, Atlanta, Georgia 30332, United States*

Miaofang Chi − *Center for Nanophase Materials Sciences, Oak Ridge National Laboratory, Oak Ridge, Tennessee 37831, United States;* orcid.org/0000-0003-0764-1567

Complete contact information is available at: https://pubs.acs.org/10.1021/acs.nanolett.1c05009

Notes

The authors declare no competing financial interest.

■ ACKNOWLEDGMENTS

This work was supported in part by a grant from the NSF (CHE 2105602) and start-up funds from the Georgia Institute of Technology. This work was performed in part at the Georgia Tech Institute for Electronics and Nanotechnology, a member of the National Nanotechnology Coordinated Infrastructure (NNCI), which is supported by the National Science Foundation (ECCS-2025462). H.C. and M.C. were supported by the U.S. Department of Energy (DOE), Office of Sciences, under early career Award No. ERKCZ55. Microscopy research was supported by the Center for Nanophase Materials Sciences (CNMS), which is a U.S. DOE, Office of Science User Facility at Oak Ridge National Laboratory.

■ REFERENCES

(1) Shi, Y.; Lyu, Z.; Zhao, M.; Chen, R.; Nguyen, Q. N.; Xia, Y. Noble-Metal Nanocrystals with Controlled Shapes for Catalytic and Electrocatalytic Applications. *Chem. Rev.* **2021**, *121*, 649−735.

(2) Jones, M. R.; Osberg, K. D.; Macfarlane, R. J.; Langille, M. R.; Mirkin, C. A. Templated Techniques for the Synthesis and Assembly of Plasmonic Nanostructures. *Chem. Rev.* **2011**, *111*, 3736−3827.

(3) Wei, Q.; Wu, S.; Sun, Y. Quantum-Sized Metal Catalysts for Hot-Electron-Driven Chemical Transformation. *Adv. Mater.* **2018**, *30*, 1802082.

(4) Jin, M.; Zhang, H.; Xie, Z.; Xia, Y. Palladium nanocrystals enclosed by {100} and {111} facets in controlled proportions and their catalytic activities for formic acid oxidation. *Energy Environ. Sci.* **2012**, *5*, 6352−6357.

(5) Choi, S.-I.; Herron, J. A.; Scaranto, J.; Huang, H.; Wang, Y.; Xia, X.; Lv, T.; Park, J.; Peng, H.-C.; Mavrikakis, M.; Xia, Y. A Comprehensive Study of Formic Acid Oxidation on Palladium Nanocrystals with Different Types of Facets and Twin Defects. *ChemCatChem.* **2015**, *7*, 2077−2084.

(6) Xia, X.; Choi, S.-I.; Herron, J. A.; Lu, N.; Scaranto, J.; Peng, H.-C.; Wang, J.; Mavrikakis, M.; Kim, M. J.; Xia, Y. Facile Synthesis of Palladium Right Bipyramids and Their Use as Seeds for Overgrowth and as Catalysts for Formic Acid Oxidation. *J. Am. Chem. Soc.* **2013**, *135*, 15706−15709.

(7) Janssen, A.; Nguyen, Q. N.; Xia, Y. Colloidal Metal Nanocrystals with Metastable Crystal Structures. *Angew. Chem., Int. Ed.* **2021**, *60*, 12192−12203.

(8) Bueno, S. L. A.; Ashberry, H. M.; Shafei, I.; Skrabalak, S. E. Building Durable Multimetallic Electrocatalysts from Intermetallic Seeds. *Acc. Chem. Res.* **2021**, *54*, 1662−1672.

(9) Shen, T.; Yang, Y.; Xu, X. Structure−Reactivity Relationship for Nano-Catalysts in the Hydrogenation/Dehydrogenation Controlled Reaction Systems. *Angew. Chem., Int. Ed.* **2021**, *60*, 26342−26345.

(10) Cheng, H.; Yang, N.; Lu, Q.; Zhang, Z.; Zhang, H. Syntheses and Properties of Metal Nanomaterials with Novel Crystal Phases. *Adv. Mater.* **2018**, *30*, 1707189.

(11) Han, S.; Xia, G.-J.; Cai, C.; Wang, Q.; Wang, Y.-G.; Gu, M.; Li, J. Gas-assisted transformation of gold from fcc to the metastable 4H phase. *Nat. Commun.* **2020**, *11*, 552.

(12) Huang, X.; Li, S.; Huang, Y.; Wu, S.; Zhou, X.; Li, S.; Gan, C. L.; Boey, F.; Mirkin, C. A.; Zhang, H. Synthesis of hexagonal close-packed gold nanostructures. *Nat. Commun.* **2011**, *2*, 292.

(13) Liu, X.; Luo, J.; Zhu, J. Size Effect on the Crystal Structure of Silver Nanowires. *Nano Lett.* **2006**, *6*, 408−412.

(14) Huang, J. L.; Li, Z.; Duan, H. H.; Cheng, Z. Y.; Li, Y. D.; Zhu, J.; Yu, R. Formation of Hexagonal-Close Packed (HCP) Rhodium as a Size Effect. *J. Am. Chem. Soc.* **2017**, *139*, 575−578.

(15) Ge, Y.; Huang, Z.; Ling, C.; Chen, B.; Liu, G.; Zhou, M.; Liu, J.; Zhang, X.; Cheng, H.; Liu, G.; Du, Y.; Sun, C.-J.; Tan, C.; Huang, J.; Yin, P.; Fan, Z.; Chen, Y.; Yang, N.; Zhang, H. Phase-Selective Epitaxial Growth of Heterophase Nanostructures on Unconventional 2H-Pd Nanoparticles. *J. Am. Chem. Soc.* **2020**, *142*, 18971−18980.

(16) Janssen, A.; Pawlik, V.; Rueden, A. D.; Xu, L.; Wang, C.; Mavrikakis, M.; Xia, Y. Facile Synthesis of Palladium-Based Nanocrystals with Different Crystal Phases and a Comparison of Their Catalytic Properties. *Adv. Mater.* **2021**, *33*, 2103801.

(17) Zhao, M.; Xia, Y. Crystal-phase and surface-structure engineering of ruthenium nanocrystals. *Nat. Rev. Mater.* **2020**, *5*, 440−459.

(18) Kusada, K.; Kobayashi, H.; Yamamoto, T.; Matsumura, S.; Sumi, N.; Sato, K.; Nagaoka, K.; Kubota, Y.; Kitagawa, H. Discovery of face-centered-cubic ruthenium nanoparticles: facile size-controlled synthesis using the chemical reduction method. *J. Am. Chem. Soc.* **2013**, *135*, 5493−6.

(19) Araki, N.; Kusada, K.; Yoshioka, S.; Sugiyama, T.; Ina, T.; Kitagawa, H. Observation of the Formation Processes of Hexagonal Close-packed and Face-centered Cubic Ru Nanoparticles. *Chem. Lett.* **2019**, *48*, 1062−1064.

(20) Fan, Z.; Zhang, H. Template Synthesis of Noble Metal Nanocrystals with Unusual Crystal Structures and Their Catalytic Applications. *Acc. Chem. Res.* **2016**, *49*, 2841−2850.

(21) Ye, H.; Wang, Q.; Catalano, M.; Lu, N.; Vermeylen, J.; Kim, M. J.; Liu, Y.; Sun, Y.; Xia, X. Ru Nanoframes with an fcc Structure and Enhanced Catalytic Properties. *Nano Lett.* **2016**, *16*, 2812−7.

(22) Zhao, M.; Figueroa-Cosme, L.; Elnabawy, A. O.; Vara, M.; Yang, X.; Roling, L. T.; Chi, M.; Mavrikakis, M.; Xia, Y. Synthesis and Characterization of Ru Cubic Nanocages with a Face-Centered Cubic Structure by Templating with Pd Nanocubes. *Nano Lett.* **2016**, *16*, 5310−7.

(23) Zhao, M.; Elnabawy, A. O.; Vara, M.; Xu, L.; Hood, Z. D.; Yang, X.; Gilroy, K. D.; Figueroa-Cosme, L.; Chi, M.; Mavrikakis, M.; Xia, Y. Facile Synthesis of Ru-Based Octahedral Nanocages with Ultrathin Walls in a Face-Centered Cubic Structure. *Chem. Mater.* **2017**, *29*, 9227−9237.

(24) Zhao, M.; Xu, L.; Vara, M.; Elnabawy, A. O.; Gilroy, K. D.; Hood, Z. D.; Zhou, S.; Figueroa-Cosme, L.; Chi, M.; Mavrikakis, M.; Xia, Y. Synthesis of Ru Icosahedral Nanocages with a Face-Centered-

Cubic Structure and Evaluation of Their Catalytic Properties. *ACS Catal.* **2018**, *8*, 6948−6960.
(25) Zhao, M.; Chen, Z.; Lyu, Z.; Hood, Z. D.; Xie, M.; Vara, M.; Chi, M.; Xia, Y. Ru Octahedral Nanocrystals with a Face-Centered Cubic Structure, {111} Facets, Thermal Stability up to 400 degrees C, and Enhanced Catalytic Activity. *J. Am. Chem. Soc.* **2019**, *141*, 7028−7036.
(26) McEachran, M.; Kitaev, V. Direct structural transformation of silver platelets into right bipyramids and twinned cube nanoparticles: morphology governed by defects. *ChemComm* **2008**, *44*, 5737−5739.
(27) Tan, T.; Zhang, S.; Wang, J.; Zheng, Y.; Lai, H.; Liu, J.; Qin, F.; Wang, C. Resolving the stacking fault structure of silver nanoplates. *Nanoscale* **2021**, *13*, 195−205.
(28) Gu, J.; Guo, Y.; Jiang, Y.-Y.; Zhu, W.; Xu, Y.-S.; Zhao, Z.-Q.; Liu, J.-X.; Li, W.-X.; Jin, C.-H.; Yan, C.-H.; Zhang, Y.-W. Robust Phase Control through Hetero-Seeded Epitaxial Growth for Face-Centered Cubic Pt@Ru Nanotetrahedrons with Superior Hydrogen Electro-Oxidation Activity. *J. Phys. Chem. C* **2015**, *119*, 17697−17706.
(29) Figueroa-Cosme, L.; Hood, Z. D.; Gilroy, K. D.; Xia, Y. A facile, robust and scalable method for the synthesis of Pd nanoplates with hydroxylamine as a reducing agent and mechanistic insights from kinetic analysis. *J. Mater. Chem. C* **2018**, *6*, 4677−4682.
(30) Zhao, M.; Wang, X.; Yang, X.; Gilroy, K. D.; Qin, D.; Xia, Y. Hollow Metal Nanocrystals with Ultrathin, Porous Walls and Well-Controlled Surface Structures. *Adv. Mater.* **2018**, *30*, 1801956.
(31) Xie, S.; Lu, N.; Xie, Z.; Wang, J.; Kim, M. J.; Xia, Y. Synthesis of Pd-Rh Core−Frame Concave Nanocubes and Their Conversion to Rh Cubic Nanoframes by Selective Etching of the Pd Cores. *Angew. Chem., Int. Ed.* **2012**, *51*, 10266−10270.
(32) Han, Y.; Yan, Y.; Wu, Z.; Jiang, Y.; Li, X.; Xu, Q.; Yang, X.; Zhang, H.; Yang, D. Facile synthesis of Pd@Ru nanoplates with controlled thickness as efficient catalysts for hydrogen evolution reaction. *CrystEngComm* **2018**, *20*, 4230−4236.
(33) Shriver, D.; Atkins, P. *Inorganic Chemistry*, 5th ed.; W. H. Freeman, 2009; pp 223−226.
(34) Xia, X.; Xie, S.; Liu, M.; Peng, H. C.; Lu, N.; Wang, J.; Kim, M. J.; Xia, Y. On the role of surface diffusion in determining the shape or morphology of noble-metal nanocrystals. *Proc. Natl. Acad. Sci. U.S.A* **2013**, *110*, 6669−73.
(35) Sneed, B. T.; Young, A. P.; Tsung, C. K. Building up strain in colloidal metal nanoparticle catalysts. *Nanoscale* **2015**, *7*, 12248−65.
(36) Xia, Y.; Gilroy, K. D.; Peng, H. C.; Xia, X. Seed-Mediated Growth of Colloidal Metal Nanocrystals. *Angew. Chem., Int. Ed.* **2017**, *56*, 60−95.
(37) Lide, D.; Haynes, W. CRC Handbook of Chemistry and Physics, 2009−2010, 90th ed. *J. Am. Chem. Soc.* **2009**, *131*, 12862−12862.
(38) Rodrigues, T. S.; Zhao, M.; Yang, T. H.; Gilroy, K. D.; da Silva, A. G. M.; Camargo, P. H. C.; Xia, Y. Synthesis of Colloidal Metal Nanocrystals: A Comprehensive Review on the Reductants. *Chem.-Eur. J.* **2018**, *24*, 16944−16963.
(39) Wang, X.; Choi, S. I.; Roling, L. T.; Luo, M.; Ma, C.; Zhang, L.; Chi, M.; Liu, J.; Xie, Z.; Herron, J. A.; Mavrikakis, M.; Xia, Y. Palladium-platinum core-shell icosahedra with substantially enhanced activity and durability towards oxygen reduction. *Nat. Commun.* **2015**, *6*, 7594.
(40) Lopes, P. P.; Li, D.; Lv, H.; Wang, C.; Tripkovic, D.; Zhu, Y.; Schimmenti, R.; Daimon, H.; Kang, Y.; Snyder, J.; Becknell, N.; More, K. L.; Strmcnik, D.; Markovic, N. M.; Mavrikakis, M.; Stamenkovic, V. R. Eliminating dissolution of platinum-based electrocatalysts at the atomic scale. *Nat. Mater.* **2020**, *19*, 1207−1214.
(41) Serov, A.; Kwak, C. Recent achievements in direct ethylene glycol fuel cells (DEGFC). *Appl. Catal., B* **2010**, *97*, 1−12.
(42) Zhao, M.; Lyu, Z.; Xie, M.; Hood, Z. D.; Cao, Z.; Chi, M.; Xia, Y. Pd-Ru Alloy Nanocages with a Face-Centered Cubic Structure and Their Enhanced Activity toward the Oxidation of Ethylene Glycol and Glycerol. *Small Methods* **2020**, *4*, 1900843.
(43) Xie, J.; Zhang, Q.; Gu, L.; Xu, S.; Wang, P.; Liu, J.; Ding, Y.; Yao, Y. F.; Nan, C.; Zhao, M.; You, Y.; Zou, Z. Ruthenium−platinum core−shell nanocatalysts with substantially enhanced activity and durability towards methanol oxidation. *Nano Energy* **2016**, *21*, 247−257.
(44) Chen, T.-Y.; Lee, G.-W.; Liu, Y.-T.; Liao, Y.-F.; Huang, C.-C.; Lin, D.-S.; Lin, T.-L. Heterojunction confinement on the atomic structure evolution of near monolayer core−shell nanocatalysts in redox reactions of a direct methanol fuel cell. *J. Mater. Chem. A* **2015**, *3*, 1518−1529.
(45) Alayoglu, S.; Nilekar, A. U.; Mavrikakis, M.; Eichhorn, B. Ru−Pt core−shell nanoparticles for preferential oxidation of carbon monoxide in hydrogen. *Nat. Mater.* **2008**, *7*, 333−338.
(46) Kim, H. J.; Choi, S. M.; Green, S.; Tompsett, G. A.; Lee, S. H.; Huber, G. W.; Kim, W. B. Highly active and stable PtRuSn/C catalyst for electrooxidations of ethylene glycol and glycerol. *Appl. Catal., B* **2011**, *101*, 366−375.
(47) Mahata, A.; Rawat, K. S.; Choudhuri, I.; Pathak, B. Single-layered platinum nanocage: a highly selective and efficient catalyst for fuel cells. *J. Mater. Chem. A* **2016**, *4*, 12756−12767.
(48) Liu, M.; Xie, M.; Jiang, Y.; Liu, Z.; Lu, Y.; Zhang, S.; Zhang, Z.; Wang, X.; Liu, K.; Zhang, Q.; Cheng, T.; Gao, C. Core−shell nanoparticles with tensile strain enable highly efficient electrochemical ethanol oxidation. *J. Mater. Chem. A* **2021**, *9*, 15373−15380.

Recommended by ACS

Rethinking Pseudocapacitance: A Way to Harness Charge Storage of Crystalline RuO2
Ankita Jadon, David Pech, *et al.*
MAY 04, 2020
ACS APPLIED ENERGY MATERIALS
READ

Investigating Reaction Intermediates during the Seedless Growth of Gold Nanostars Using Electron Tomography
Priscilla Choo, Teri W. Odom, *et al.*
MARCH 03, 2022
ACS NANO
READ

Deformation-Induced Phase Transformations in Gold Nanoribbons with the 4H Phase
Ade Kismarahardja, Xiaozhou Liao, *et al.*
JANUARY 24, 2022
ACS NANO
READ

Introducing Stacking Faults into Three-Dimensional Branched Nickel Nanoparticles for Improved Catalytic Activity
Zeno R. Ramadhan, Richard D. Tilley, *et al.*
JUNE 17, 2022
JOURNAL OF THE AMERICAN CHEMICAL SOCIETY
READ

Get More Suggestions >

https://doi.org/10.1021/acs.nanolett.1c05009
Nano Lett. 2022, 22, 3591−3597